Supplementary Information for

Thermal fertilization of the high-latitude northern forests

Junjie Liu[1,*], Paul Wennberg[2*], Nick Parazoo[1], Christian Frankenberg[2, 1], Yi Yin[2]

[1.] Jet Propulsion Laboratory, Caltech, US

[2.] Caltech, US

*Correspondence to: junjie.liu@jpl.nasa.gov; wennberg@caltech.edu

This PDF file includes:

Supplementary text
Figures S1 to S12
Tables S1

Supplementary Information Text

SM.1 Validation of posterior CO_2 concentration from top-down flux inversion

We validate posterior CO_2 concentration from two perspectives: seasonality and its accuracy against aircraft observations. NEE constrained by OCO-2 column CO_2 observations is used to calculate TER together with SIF-constrained GPP. Therefore, it is important for the posterior NEE to capture the observed seasonal cycle amplitude. Here we compare the CO_2 seasonal cycle amplitude constrained by OCO-2 observations with the observed CO_2 SCA at Mauna Loa (MLO), which represents hemispheric signal. The posterior CO_2 seasonal cycle amplitude sampled at Mauna Loa stations agree with the observations within uncertainty as shown in Figure S3. To calculate the uncertainty of the CO_2 SCA, we calculate an ensemble of CO_2 SCA based on ~10% of randomly sampled subset data. The mean and uncertainties of the CO_2 SCA are based on 1000 samples.

To further validate posterior NEE constrained by OCO-2 column CO_2 observations, we compare the posterior CO_2 concentrations from top-down flux inversion against independent aircraft observations north of 30°N collected between 2015-2017 (Table S1). Figure S31 C shows the distribution of aircraft observations, most of which are over NA. We sample posterior CO_2 concentrations along aircraft tracks, and then compare monthly regional mean values against aircraft observations between April and September over 2015-2017 in the bottom panel of Figure S3. Compared to the aircraft observations, the bias is -0.12ppm, and the root mean square (RMS) error is 0.37ppm.

SM.2 Calculation of CO_2 seasonal cycle amplitude (SCA) at surface sites

To calculate seasonal cycles at the four high latitude surface sites, we fit the following functions to surface data with "*nlinfit*" function in Matlab:

$$f = a(1) \times dt + a(2) \times dt^2 + a(3) + a(4) \times sin\big(2\pi \times dt + a(5)\big) + a(6) \times sin\big(4\pi \times dt + a(7)\big) + a(8) \times sin\big(6\pi \times dt + a(9)\big) + a(10) \times sin\big(8\pi \times dt + a(11)\big)$$

(Equation 2)

Where *dt* is the time interval with fraction of a year as unit, and a(:) are the coefficents.

After removing the trend and intercept (i.e., the first three terms) from the raw data, we fit a four-harmonic (the last four terms in equation 2) curve for the data, and calculate the CO_2 seasonal cycle amplitude (SCA) every four years. We fit a linear trend to the CO_2 SCA, and calculate one sigma uncertainty of the linear trend. We follow the same procedure to calculate model simulated CO_2 seasonal cycle amplitude and its trend. Summary of the SCA trend and uncertainties for both observations and models are shown in Figure 4.

SM.3 **Calculation of CO_2 seasonal cycle amplitude and uncertainty during International Geophysical Year (IGY) and HIPPO**

We quantify the contributions of NEE SCA changes between 50°N and 75°N (resulting from the increase in temperature alone) to the increase of CO_2 SCA for the time period of observations obtained by two aircraft campaigns: International Geophysical Year (IGY) between 1958 and 1963 and HIPPO between 2009 and 2011 (Wofsy et al., 2011). The observations are the same as Graven et al. (2013). Table S1 list the source of CO_2 observations.

To calculate CO_2 seasonal cycle amplitude of aircraft observations, we follow a procedure similar to that described in Graven et al. We only use CO_2 observations obtained near 500hPa because of sparse aircraft observations ~ 700hPa. The IGY CO_2 observations were detrended to remove the 0.72 ppm/year linear trend derived from Mauna Loa (MLO) observations. A linear trend, calculated from MLO observations, was similarly removed from HIPPO observations. Finally, the observations were binned to 10-degree latitude bands between 15°N and 75°N, and into a 15-degree latitude band for 75°N-90°N.

As in Graven et al., we calculate the specific shape of CO_2 seasonal amplitude over each latitude band sampled by the NOAA's aircraft observations using flask data from four ground stations: Molokai Island, Hawaii (HAA, 21°N), Trinidad Head, California (THD, 41°N), Estevan Point, British Columbia (ESP, 50°N), and Poker Flat, Alaska (PFA, 65°N). After removing the linear trend (calculated from MLO observations), we fit a three harmonics at each aircraft location.

Following Graven et al., we assume the same seasonal cycle shape at each latitude band when we calculate the CO_2 seasonal amplitude for IGY and HIPPO aircraft observations. We only fit a gain parameter to best fit the observations. Observed CO_2 SCA in 1958-1963 (black) and in 2009-2011 (blue) over seven latitude bands is shown in the top left panel in Figure S12, and its change is shown as solid magenta in the bottom right panel in Figure S12.

We follow the same procedure to calculate CO_2 seasonal cycle with CO_2 simulations forced by predicted ensemble NEE. The top right in Figure S12 shows the CO2 SCA forced by ensemble predicted CO_2 monthly NEE over 50°N and 75 °N in 1958-1963 (black) and in 2009-2011 (blue).

To calculate uncertainties of the observed CO_2 SCA we use a bootstrap method. We generate 1000 random samples of original data for each latitude bin, with each sample including one-third of the original data. The standard deviations of the CO_2 SCA from these 1000 samples are the uncertainties shown in the top left panel of Figure S12. We approximate the percentage contribution of boreal forest to CO_2 SCA changes observed by IGY and HIPPO with the ratio between observational-constrained CO_2 SCA in 1958-1963 and the observed CO_2 SCA in 1958-1963, which is shown in the bottom left in Figure S13. The uncertainty of bottom left panel in Figure S12 is the propagation of uncertainties from observed CO_2 SCA and the predicted CO_2 SCA in top right panel of Figure S12. The dashed magenta line in bottom right panel of Figure S12 and Figure 4 in the main text is the multiplication between observed CO_2 SCA changes and the approximate contributions of the boreal forest to CO_2 SCA observed by IGY and HIPPO.

The uncertainty of predicted CO_2 SCA changes shown in Figure 4 is the square root of as the sum variance of predicted CO_2 SCA in 1958-1963 and 2009-2011.

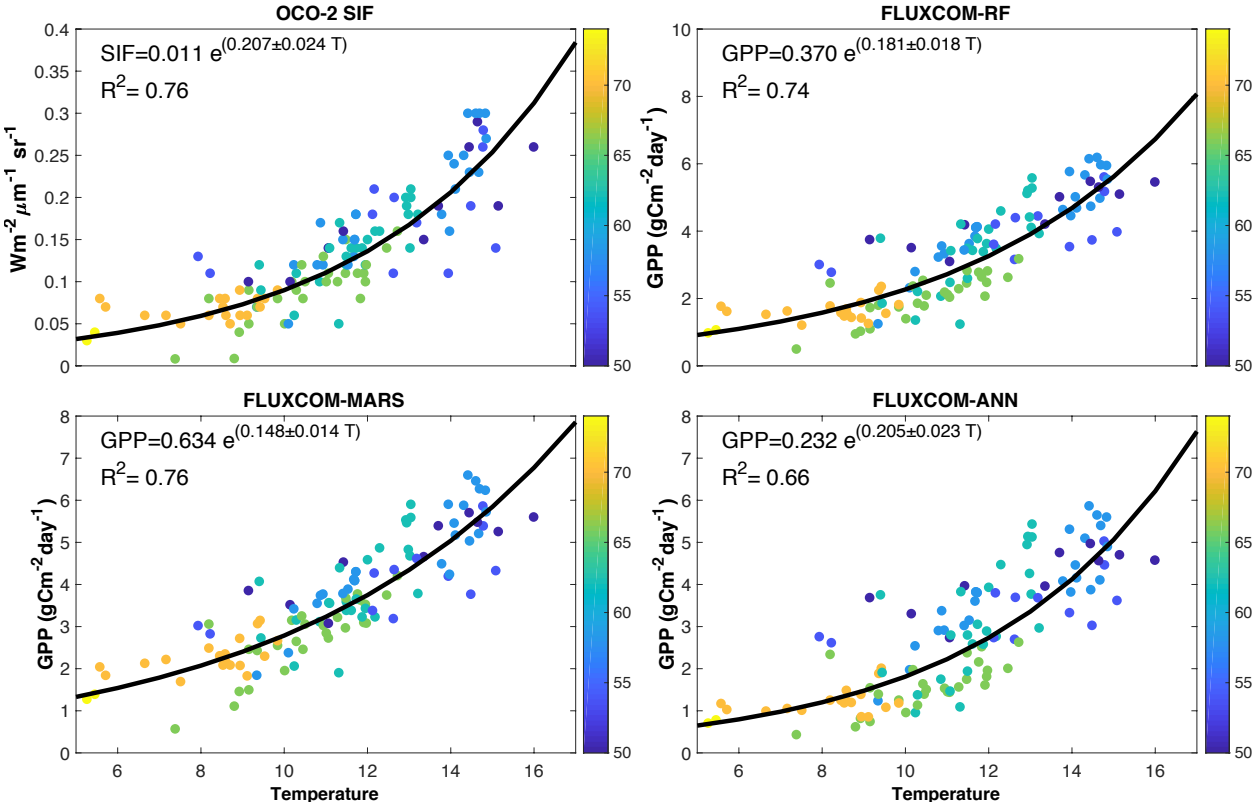

Figure S1 Growing season mean SIF ($Wm^{-2}\mu m^{-1}sr^{-1}$) vs. growing season mean temperature (top left panel) and the growing season mean GPP ($gCm^{-2}day^{-1}$) vs. temperature (Celsius) based on three FLUXCOM GPP products (top right and the bottom two panels) over 50°N-75°N. Each point has tree coverage larger than 40%. The uncertainty is 3σ. The temperature is 2-meter air temperature from ERA-interim reanalysis (Table S1).

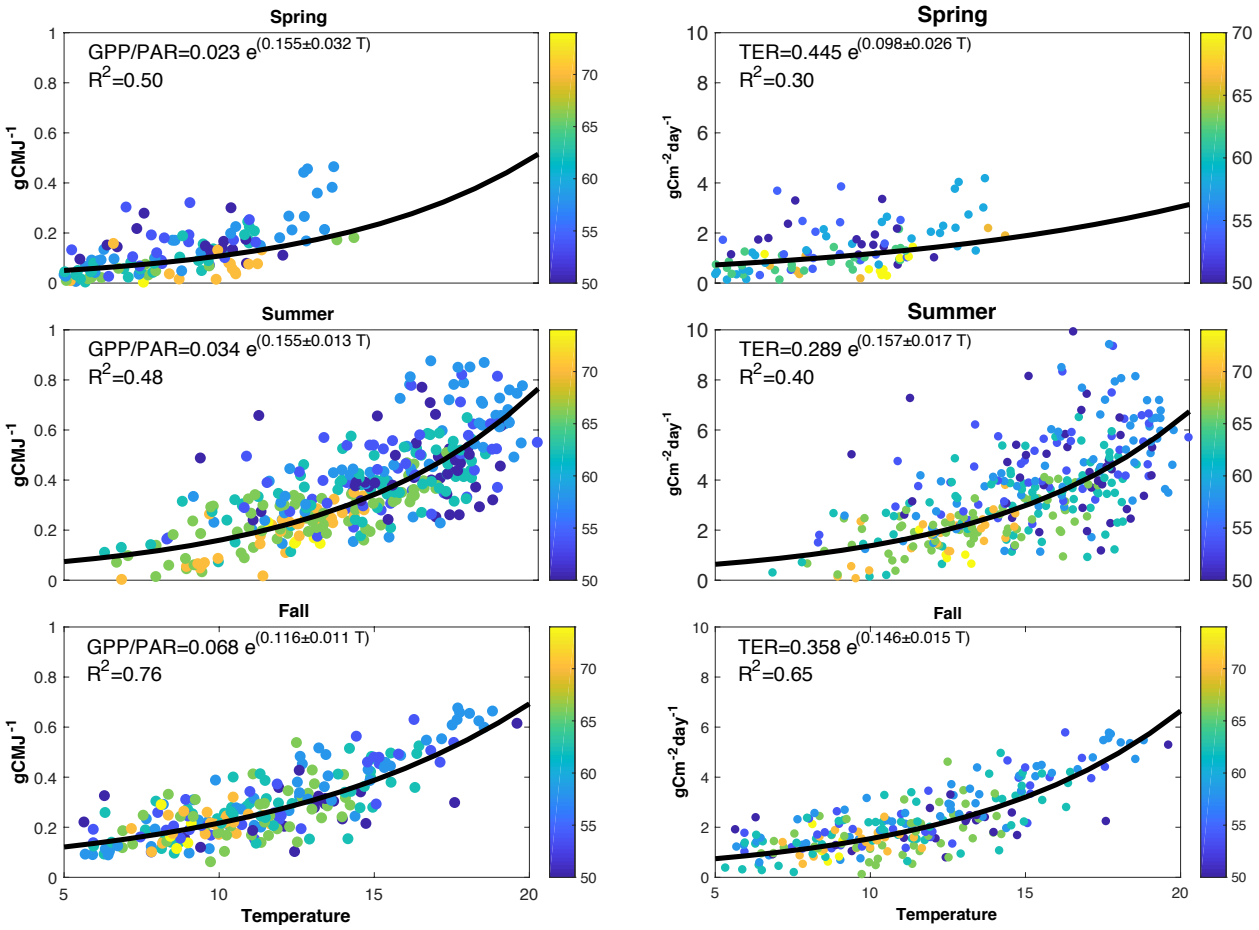

Figure S2 GPP/PAR vs. temperature (left column) and TER vs. temperature (right column) for spring (top), summer (middle), and fall (bottom) months. The color bars indicate latitudes. The uncertainty is 3σ of the exponential fitting.

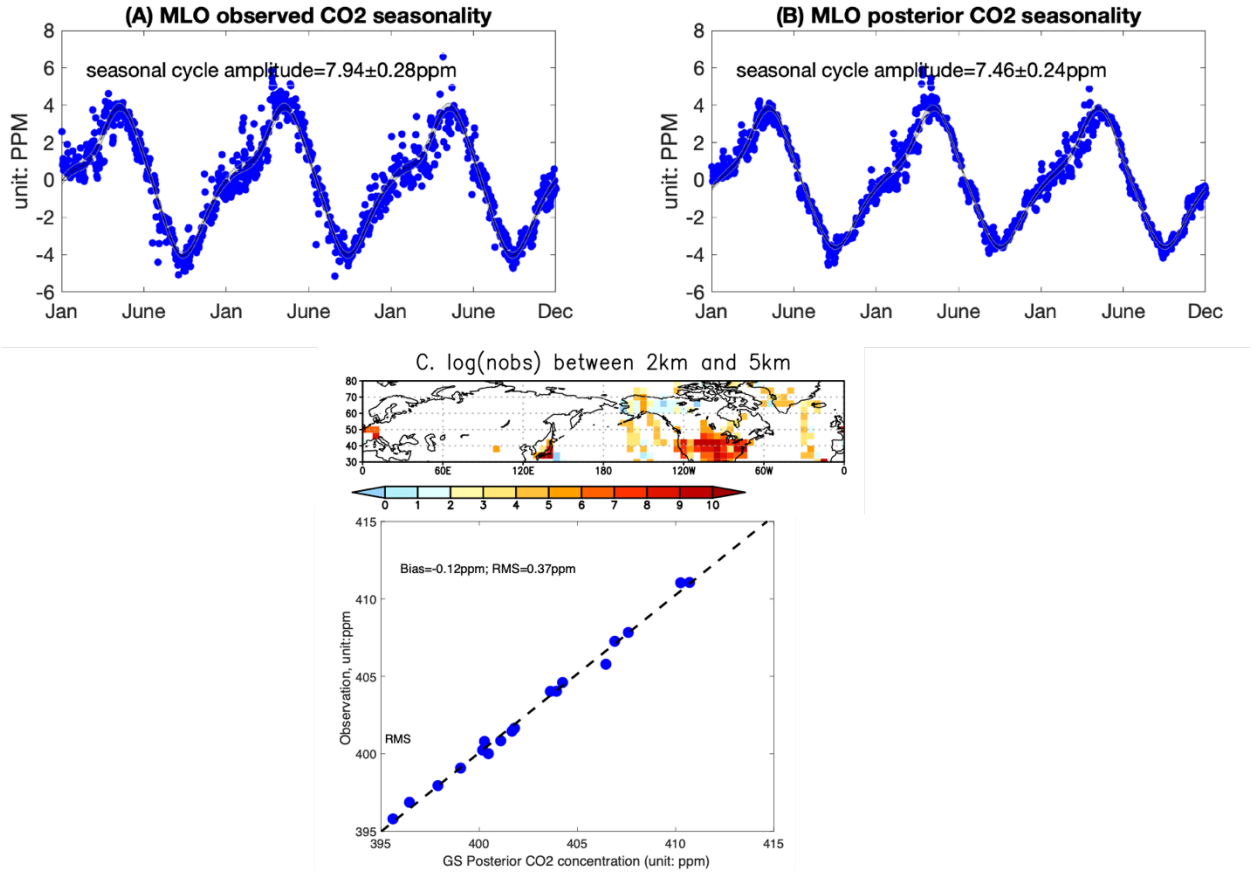

Figure S3 The CO_2 seasonal cycle from Jan 2015 to the end of 2017 based on CO_2 observations at MLO (A) and posterior CO_2 concentration sampled at MLO (B). The blue dots are the original data points, and the black lines with grey shades are the seasonal cycle fitting and its uncertainties. (C): the total number of aircraft observations between 2 kilometers (km) and 5 km (unit: log) between 2015 and 2017. Bottom: the posterior CO_2 concentration (x-axis) sampled at aircraft observations vs. aircraft CO_2 observations. Each point is a regional monthly mean value between April and September from 2015 to 2017. The CO_2 observations are from ObsPack (https://www.esrl.noaa.gov/gmd/ccgg/obspack/data.php?id=obspack_co2_1_OCO2MIP_v2.1_2019-08-15)

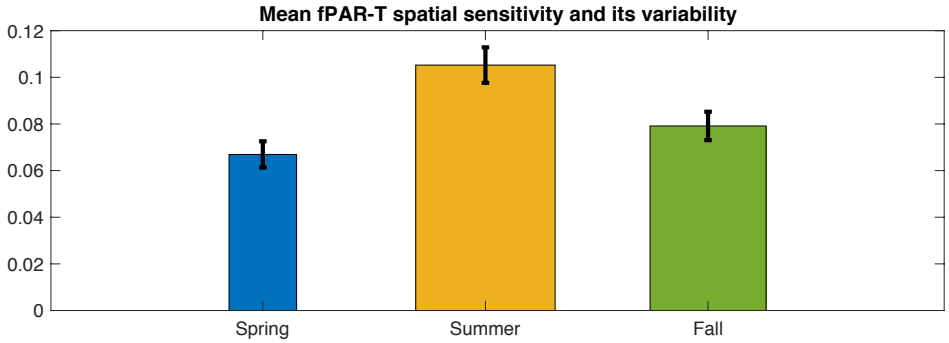

Figure S4 Mean observed fPAR-T spatial sensitivity and its variability over eight 4-year groups from 1982. The width of the bar is proportional to the R^2 value of the spatial fitting between fPAR and temperature. The R^2 are 0.4, 0.6 and 0.5 for spring, summer, and fall respectively (Figure S4). The fPAR is from GIMMS3g (Table S1).

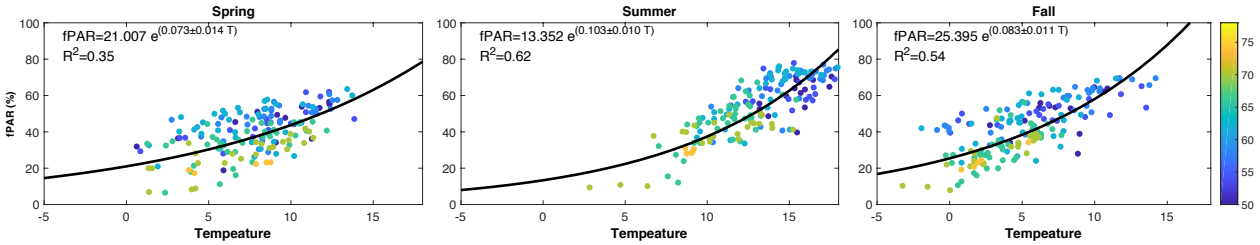

Figure S5 The fPAR – temperature spatial relationship during spring (left), summer (middle), and fall (right) based on fPAR over 2013-2016. The fPAR is from GIMMS 3g. The temperature is CRU 2-meter air temperature.

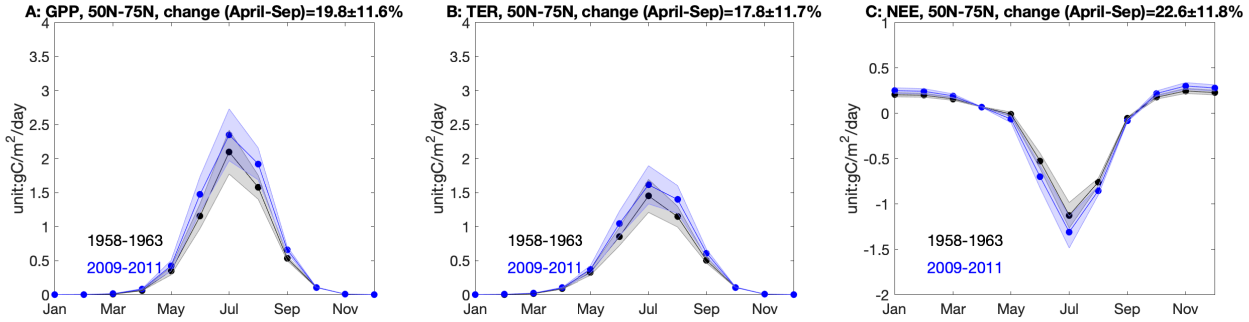

Figure S6 Hindcast monthly mean GPP (A), TER (B), and NEE (C) seasonal cycles and its uncertainties over 50°N- 75°N for 1958-1963 (black line with grey shades) and 2009-2011 (blue line with blue shades). The uncertainties are based on 95% shown in Figure S2.

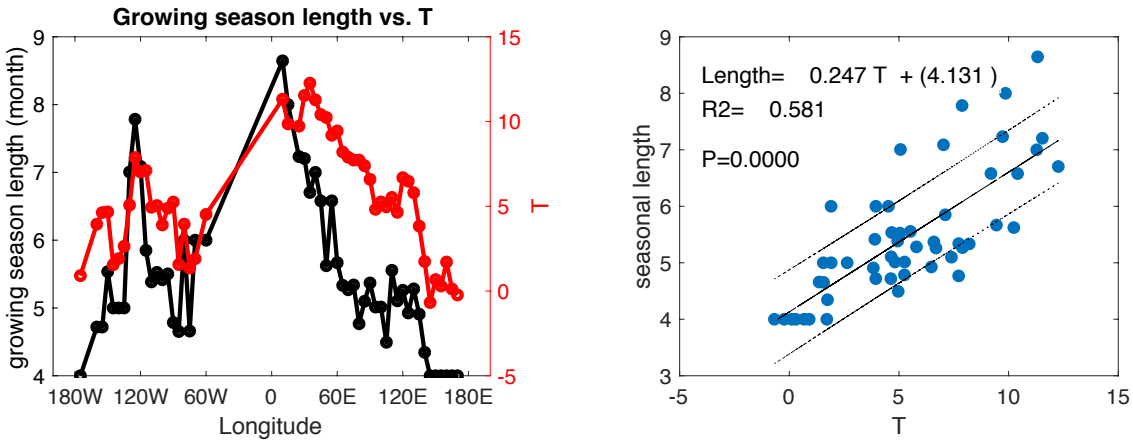

Figure S7 Left panel: latitudinal (50°N-75°N) mean growing season length (black) vs. monthly mean temperature (red, unit: °C) between March and September as a function of longitude. Right panel: scatter plot of monthly mean temperature between March and September (unit: °C) and the growing seasonal length (unit: months) as each 5° longitude. The R^2 is 0.58.

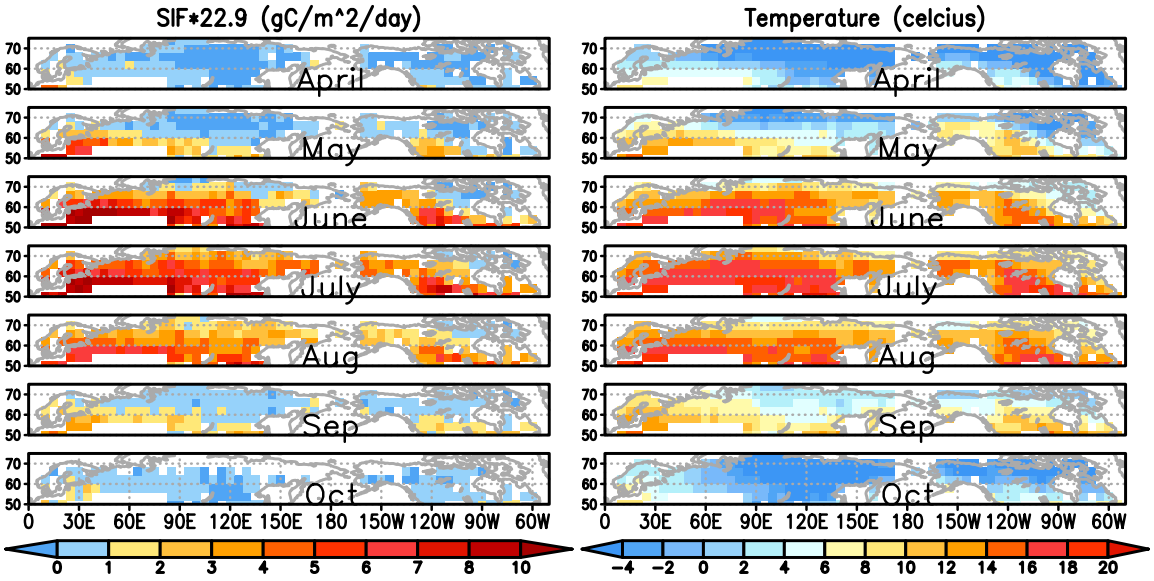

Figure S8 Monthly mean GPP (average over 2015-2017) (22.9 times of the solar induced chlorophyll fluorescence) (unit: $gCm^{-2}day^{-1}$) and mean temperature (2015-2017) from April to October (from the top to the bottom).

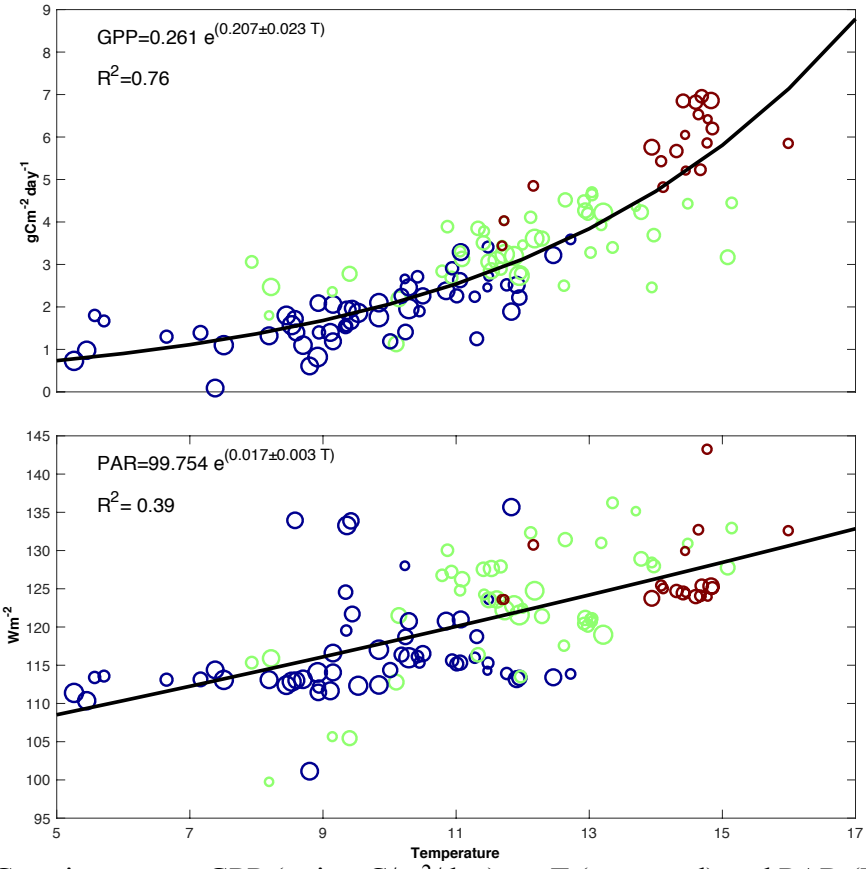

Figure S9 Growing season GPP (unit: gC/m^2/day) vs. T (top panel) and PAR (W/m^2) vs. T (bottom panel). Brown: deciduous broadleaf forest; green: needle leaf forest; blue: shrubland. The uncertainty is 3σ. The temperature is 2-meter air temperature from ERA-interim (Table S1).

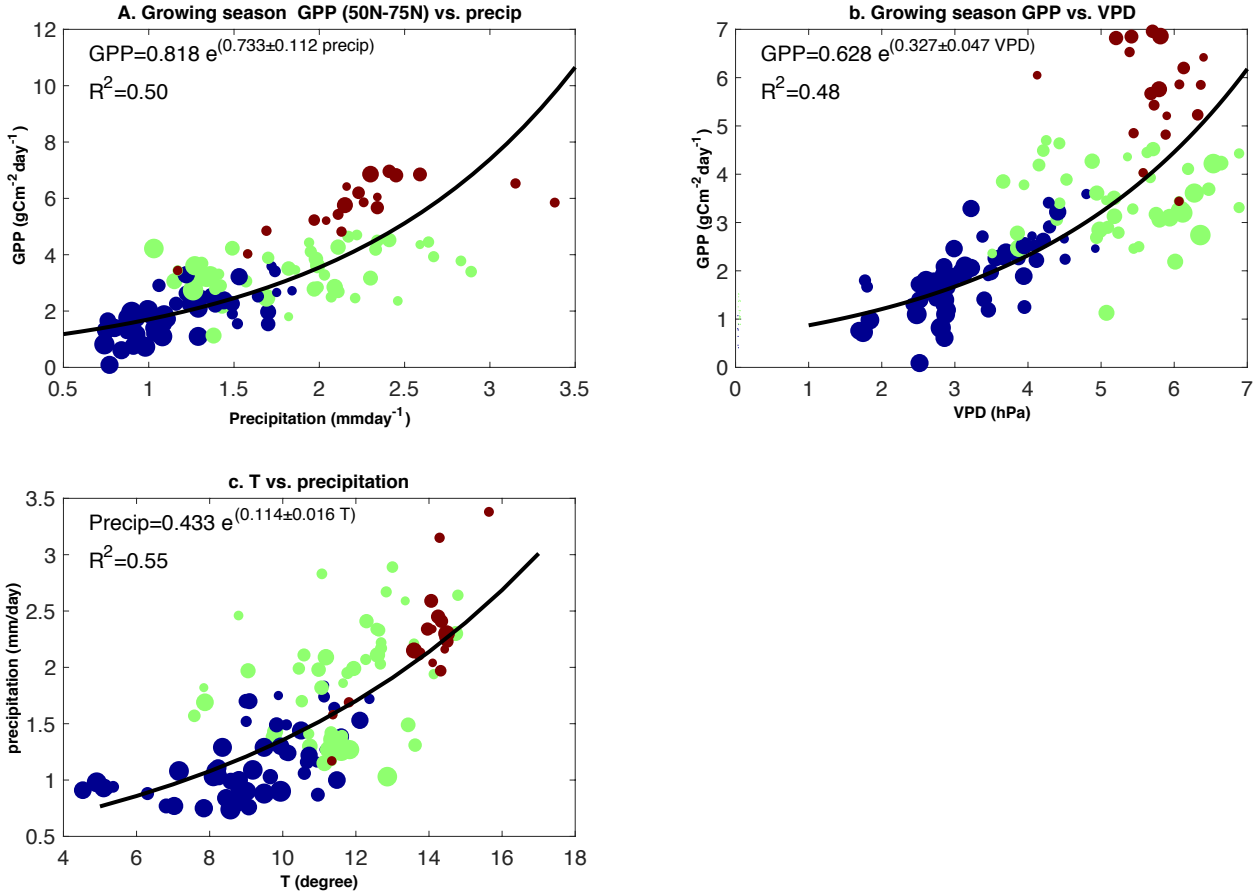

Figure S10 Sensitivity of GPP to precipitation (a) (unit: mm/day) and to vapor pressure deficit (VPD) (b). The relationship between growing season mean temperature and precipitation (c). The VPD is calculated with temperature and relative humidity from ERA-interim. The precipitation is CPC Merged Analysis of Precipitation (Table S1)

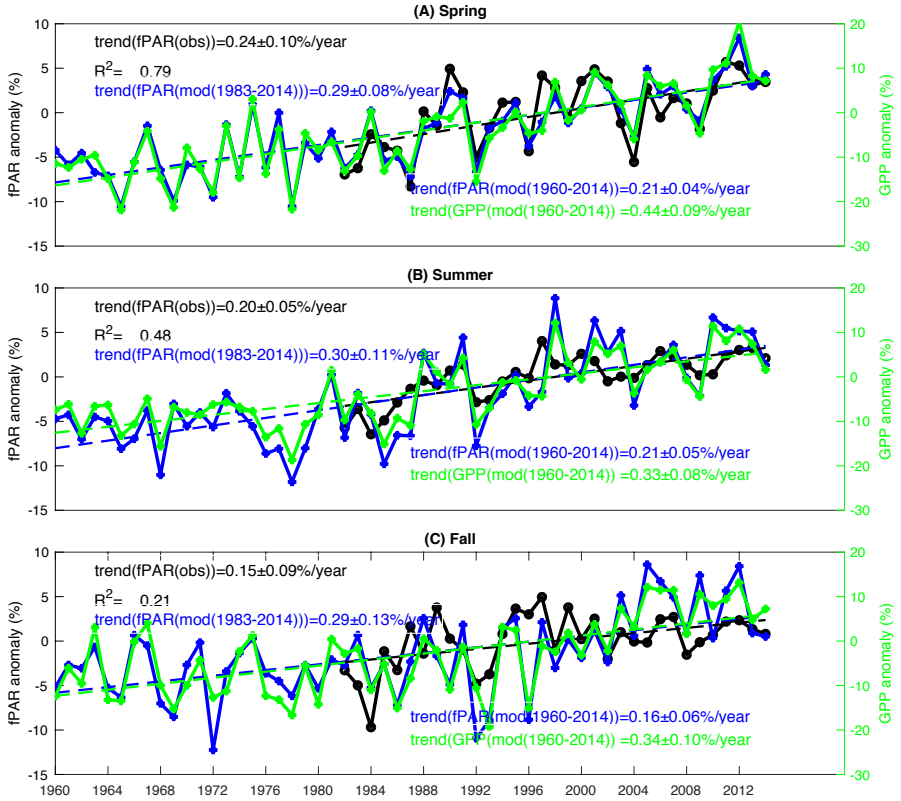

Figure S11 Seasonal hindcast of GPP and fPAR between 1960 and 2014**.** Seasonal fPAR and GPP anomaly and trend. (A): spring; (B): summer, and (C): Fall. Black: observed fPAR anomaly and trend (dashed line); blue: hindcast fPAR anomaly and trend (%); green: hindcast GPP anomaly (%) and trend (dashed line). The mean values for each variable are the average between 1983 and 2014. The uncertainty is 3σ of the linear fitting. The fPAR observations are from GIMMS3g.

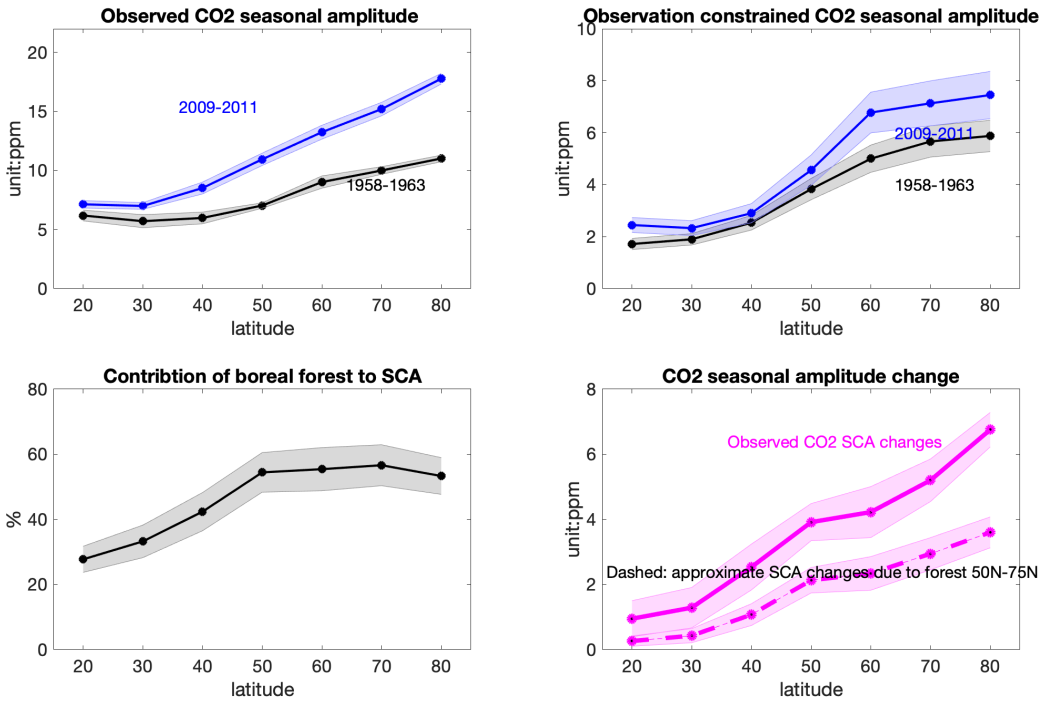

Figure S12 Top left panel: observed CO_2 seasonal cycle amplitude at 500hPa based on IGY (1958-1963) (black) and HIPPO (2009-2011) (blue lines) aircraft campaigns; top right panel: the corresponding model simulated seasonal cycle amplitude forced by hindcast forest NEE over 50°N-75°N. Bottom left panel: the contributions of boreal forest to the CO_2 SCA at each latitude bands, which is the ratio between model simulated CO_2 SCA forced by forest NEE over 50°N-75°N and the observed CO_2 SCA. Bottom right panel: the changes of observed CO_2 SCA at each latitude bands (solid magenta), and the approximate CO_2 SCA changes due to changes of forest NEE over 50°N and 75°N (dashed magenta), which is the multiplication between the observed CO_2 SCA changes and the percentage contribution of boreal forest to the CO_2 SCA.

Table S1 Physical variables and the data source

Variable	Source	Data link
Air Temperature	Climate Research Unit (CRU)	https://crudata.uea.ac.uk/cru/data/hrg/ cru_ts_4.03/cruts.1905011326.v4.03/
	ERA-interim	https://www.ecmwf.int/en/forecasts/datasets/reanalysis-datasets/era-interim
Photosynthetic Active Radiation (PAR)	CERES	SYN1deg product under: https://ceres.larc.nasa.gov/order_data.php
Precipitation	CPC Merged Analysis of Precipitation Standard	ftp.cpc.ncep.noaa.gov precip/cmap/monthly
Fraction of PAR	MODIS (2003-2017) MCD15A3H_006	https://lpdaac.usgs.gov/product_search/ ?collections=Combined+MODIS& collections=Terra+MODIS&collections =Aqua+MODIS&view=list
	AVHRR (1982-2016)	GIMMS3g
Surface CO_2 sites: Alert, Canada (ALT), Cold Bay, Alaska (CBA), Barrow, Alaska (BRW), and Shemya Island (SHM)	NOAA	https://www.esrl.noaa.gov/gmd/dv/data/
CO_2 from IGY aircraft campaign		https://scrippsco2.ucsd.edu/data/atmospheric_co2/aircraft_campaign_data.html
CO_2 from HIPPO		http://hippo.ornl.gov/
Aircraft CO2 observations (2005-2011)	NOAA	https://www.esrl.noaa.gov/gmd/ccgg/obspack/
Aircraft CO2 observations between 2015 and 2017	NOAA	CO2 observations are from ObsPack (https://www.esrl.noaa.gov/gmd/ccgg/obspack/data.php?id=obspack_co2_1_OCO2MIP_v2.1_2019-08-15
Solar Induced Chlorophyll Fluorescence (SIF)	OCO-2	https://disc.gsfc.nasa.gov/datasets/ OCO2_L2_Lite_SIF_8r/summary? keywords=OCO-2%20SIF
Column CO_2 observations	OCO-2 b-9	https://co2.jpl.nasa.gov/#mission=OCO-2
FLUXCOM GPP	FLUXCOM	http://www.fluxcom.org
Top-down NEE fluxes between 2015 and 2017	Top-down CO2 flux inversion	https://data.nas.nasa.gov/carboncycle/